

Bichromatic Rabi control of semiconductor qubits

Valentin John,^{1,*} Francesco Borsoi,^{1,*} Zoltán György,^{2,*} Chien-An Wang,¹ Gábor Széchenyi,² Floor van Riggelen,¹ William I. L. Lawrie,¹ Nico W. Hendrickx,¹ Amir Sammak,³ Giordano Scappucci,¹ András Pályi,^{4,5,†} and Menno Veldhorst^{1,†}

¹*QuTech and Kavli Institute of Nanoscience, Delft University of Technology,
P.O. Box 5046, 2600 GA Delft, The Netherlands*

²*Institute of Physics, Eötvös University, H-1117 Budapest, Hungary*

³*QuTech and Netherlands Organisation for Applied Scientific Research (TNO), Stieltjesweg 1, 2628 CK Delft*

⁴*Department of Theoretical Physics, Institute of Physics,
Budapest University of Technology and Economics, Műegyetem rkp. 3., H-1111 Budapest, Hungary*

⁵*MTA-BME Quantum Dynamics and Correlations Research Group,
Budapest University of Technology and Economics, Műegyetem rkp. 3., H-1111 Budapest, Hungary*

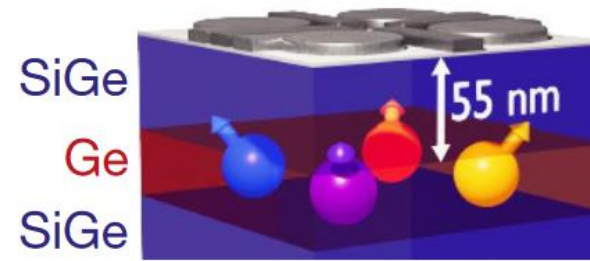
(Dated: August 4, 2023)

<https://arxiv.org/abs/2308.01720>

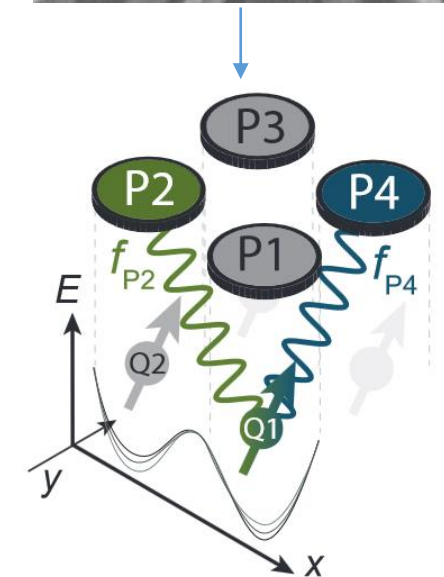
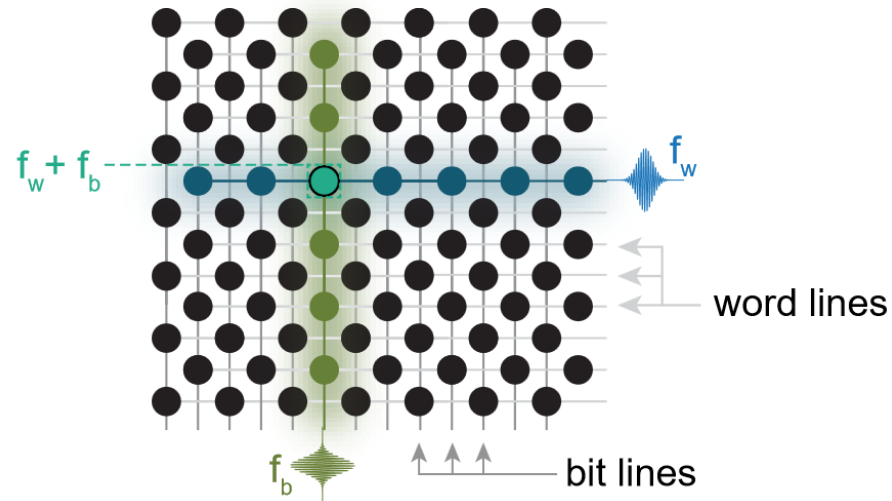
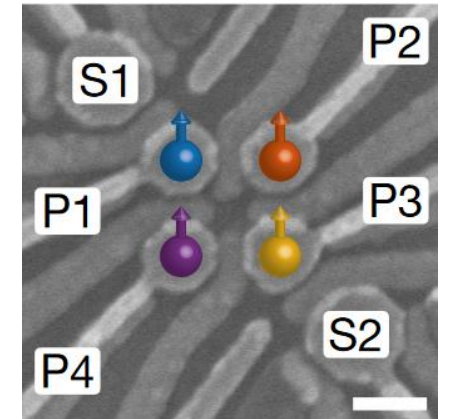
Journal Club, 15.12.2023

Device & setup

- 4-Qubit device (holes in strained Ge QW)
- Single hole in each quantum dot
- Focus on Q1 and Q2; Q3/4 remain in ground state
- Reflectometry on charge sensors S1/2
- AC detuning modulation \rightarrow qubit rotations
- Bichromatic control – potential application:
2 microwave tones, f_w , f_b , target rotations of qubit at intersection of the two lines, with
$$f_{Larmor} = f_w \pm f_b$$
- In this paper:
 - Coherent driving of qubits with mixed frequency signals
 - Investigation of resonance anticrossings



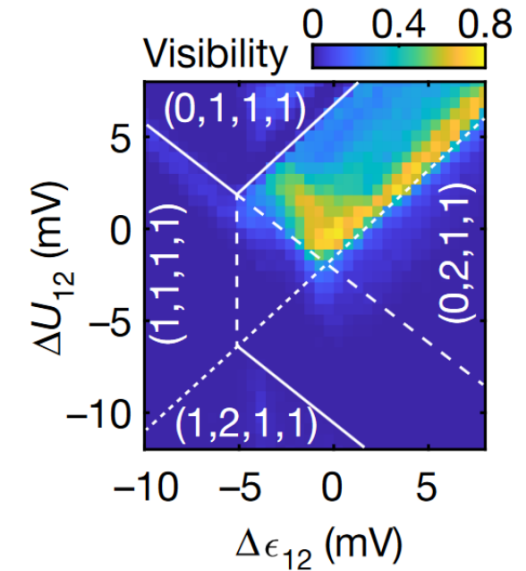
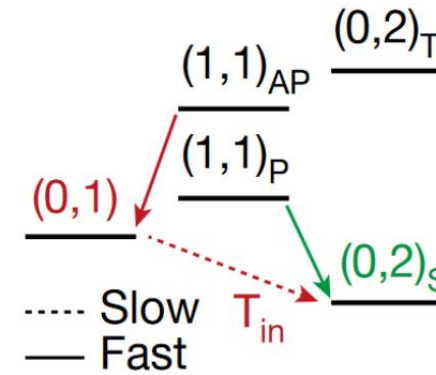
(from N. W. Hendrickx et al., Nature 2021)



Qubit readout

- Latched Pauli spin blockade readout (referring to Hendrickx et al.):
 - Pulsing from $(1,1) \rightarrow (0,2)$
 - Interdot tunneling blocked for **antiparallel** states $\xrightarrow{\text{To reservoir}} (0,1)$
 - Polarized triplet states allow holes to move to same QD $\rightarrow (0,2)_s$
 - Latching:

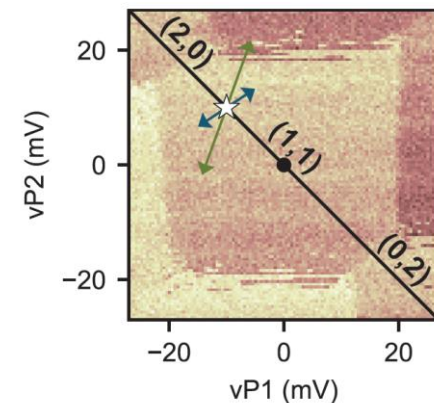
To reduce readout infidelity as a result of spin relaxation, we make use of charge latching through the reservoir^{41,42}. We achieve this effect by pulsing into the area in the $(0,2)$ charge region bounded by the extended $(1,1) - (0,1)$ (fast) and the extended $(1,1) - (1,2)$ (slow) transitions (dotted lines in Fig. 1e). When the interdot tunnelling into the $(0,2)$ charge state is blocked, the hole in the first quantum dot will quickly tunnel into the reservoir. This locks the spin state in the metastable $(0,1)$ charge state, with the decay to the $(0,2)$ ground state governed by the slow tunnelling rate T_{in} between the second quantum dot and the reservoir.



- In this paper:

- Initialization: Adiabatically pulse detuning From $(0,2) \rightarrow (1,1)$
- Manipulation: At $\epsilon_{12} = -20$ mV (white star)
- Readout: return to $(0,2)$ charge sector and perform readout

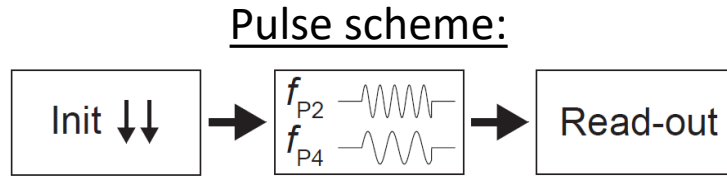
Using latched PSB



■ P2 axis — ϵ_{12}
■ P4 axis ☆ $\epsilon_{12} = -20$ mV

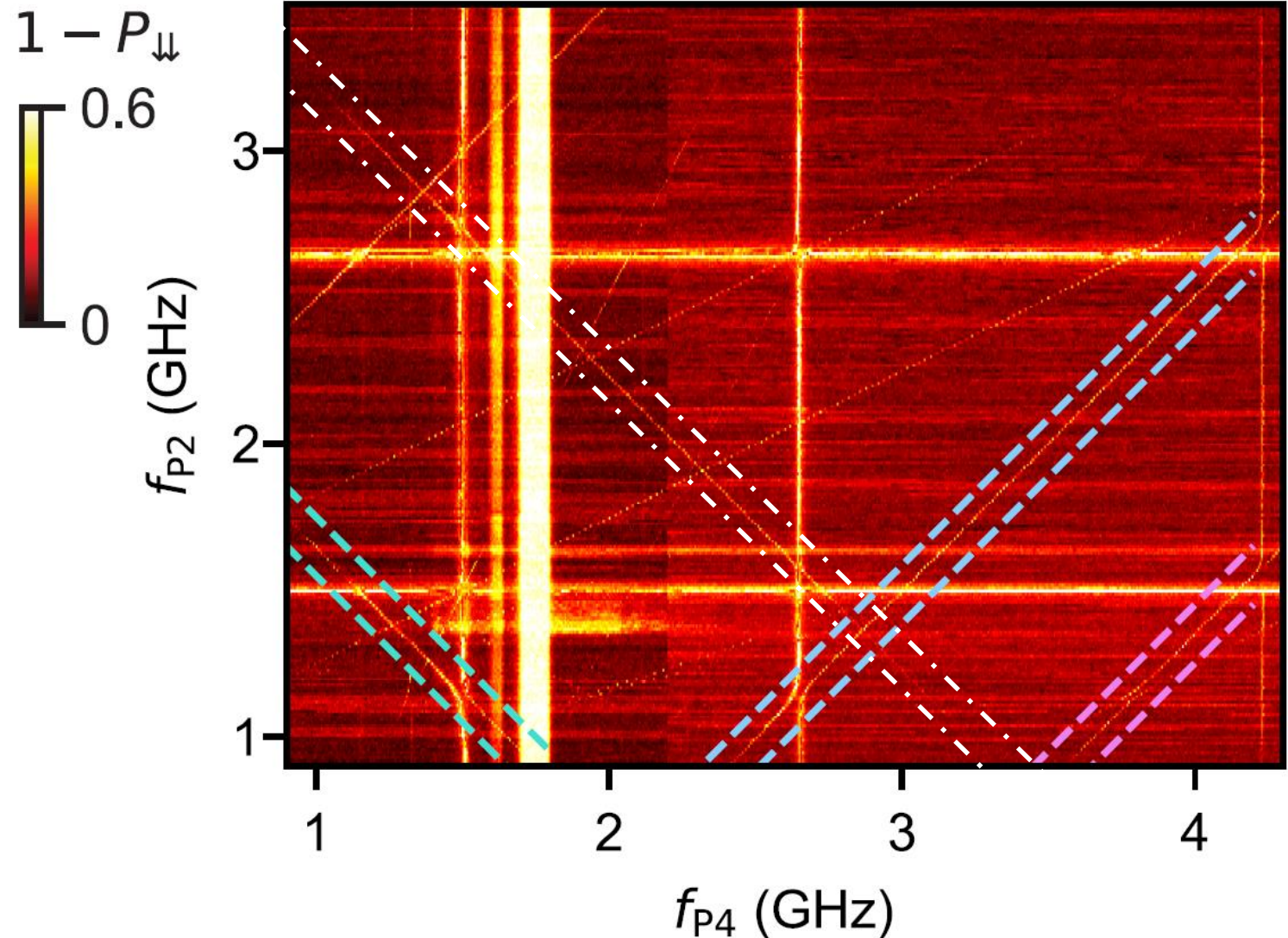
Arrows: Orientations of driving field. Amplified by factor 5
 \rightarrow P2 drive is stronger

Bichromatic EDSR spectroscopy: Overview



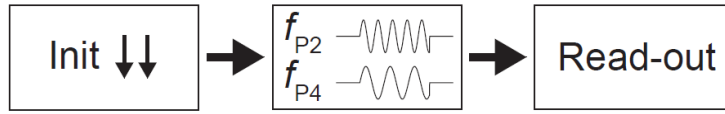
- In-plane B-field of 0.675 T
- $f_{Q1} = 1.514$ GHz, $f_{Q2} = 2.649$ GHz
- Manipulation @ $\epsilon_{12} = -20$ mV
- Monochromatic transitions: Horizontal/Vertical lines
- Bichromatic transitions: tilted resonance lines; framed by colored (+ *white*) dashed line
- Further three-photon excitations are also observed

→ Let's look at each type in detail..



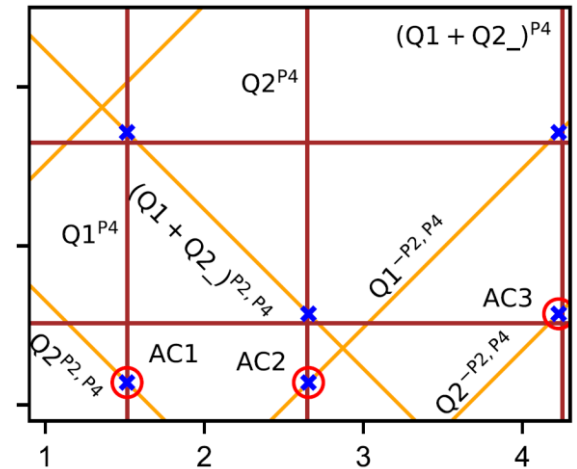
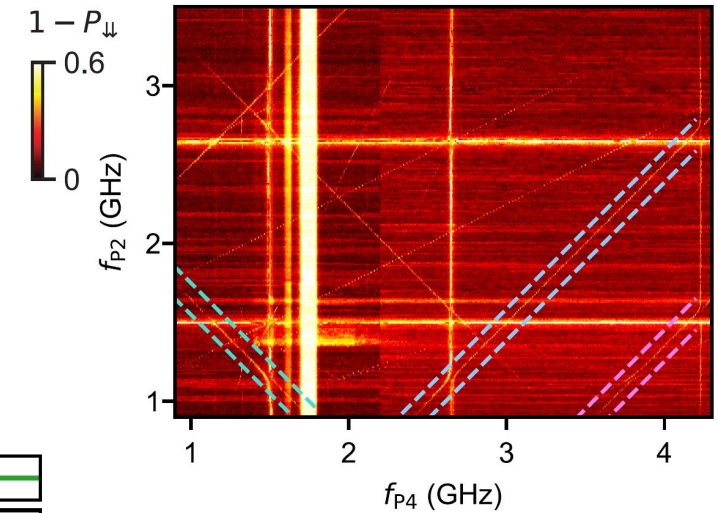
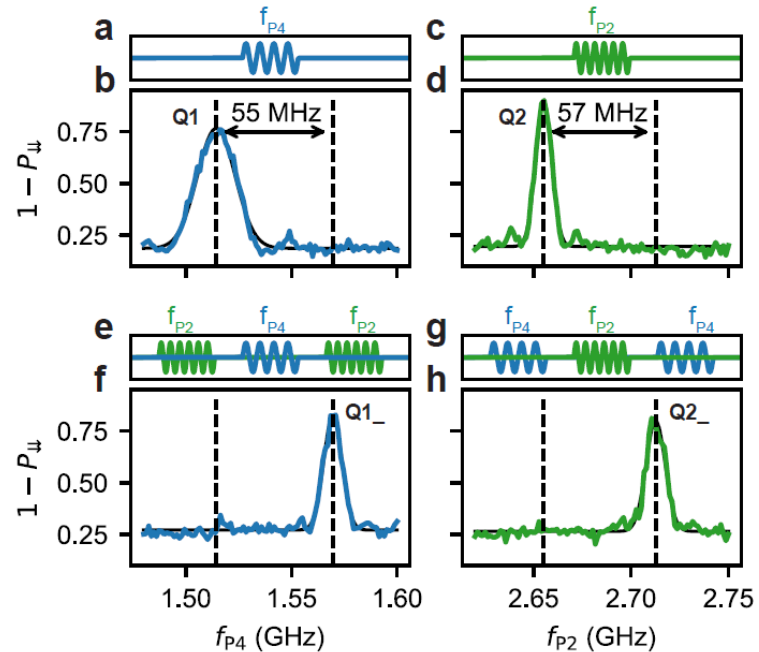
Monochromatic qubit transitions

Pulse scheme:



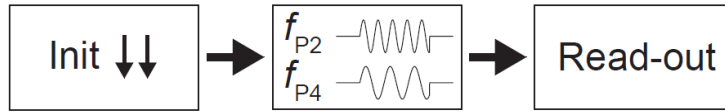
- $f_{Q1} = 1.514$ GHz, $f_{Q2} = 2.649$ GHz
- Horizontal/vertical transitions at $f_{Q1,2}$
- Q2₋ : Larmor frequency of qubit 2 when qubit 1 is in excited state
- Broad vertical excitation at $f_{P4} \approx 1.8$ GHz: transmission resonance in lines

→ Can be used to extract exchange interaction (*conditional EDSR spectroscopy*)

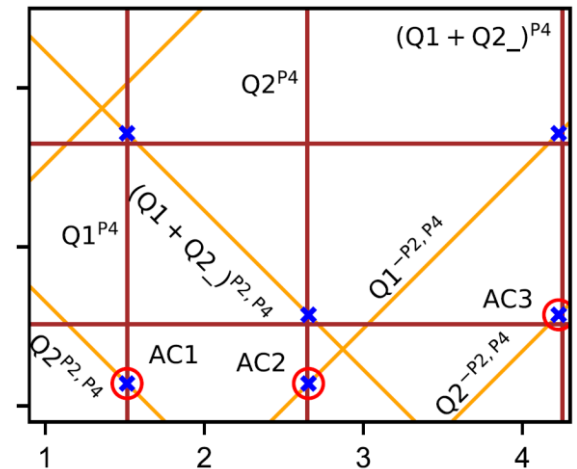
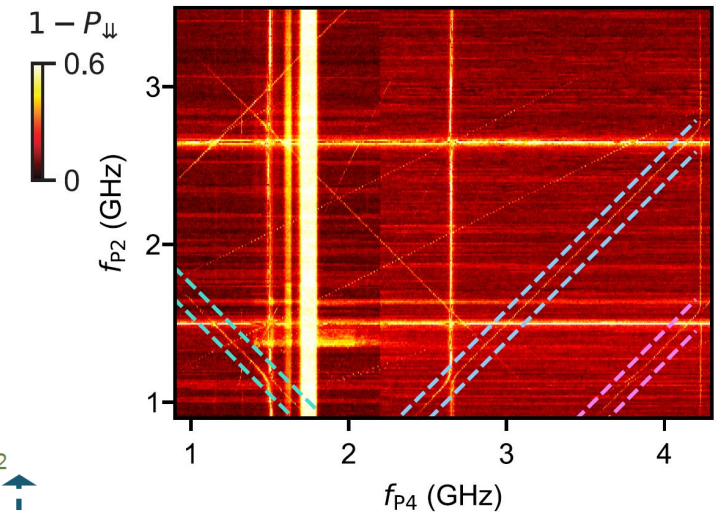
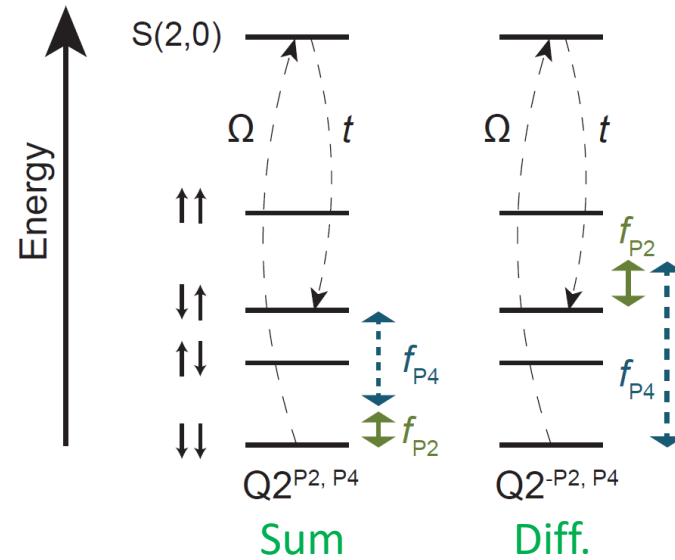


Bichromatic qubit transitions

Pulse scheme:

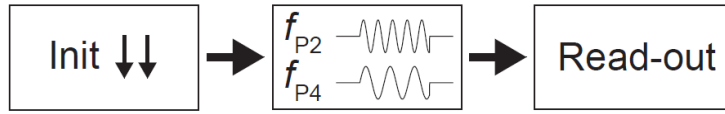


- Activated via spin-conserving (t) and spin-flipping (Ω) tunneling terms which hybridize 4 possible spin states with $S(2,0)$
- $Q1^{P2,P4}$: $f_{P4} + f_{P2} = f_{Q1}$ (not shown, high pass)
- $Q2^{P2,P4}$: $f_{P4} + f_{P2} = f_{Q2}$
- $Q1^{-P2,P4}$: $f_{P4} - f_{P2} = f_{Q1}$
- $Q2^{-P2,P4}$: $f_{P4} - f_{P2} = f_{Q2}$
- And the $(Q1 + Q2_-)$ sum term

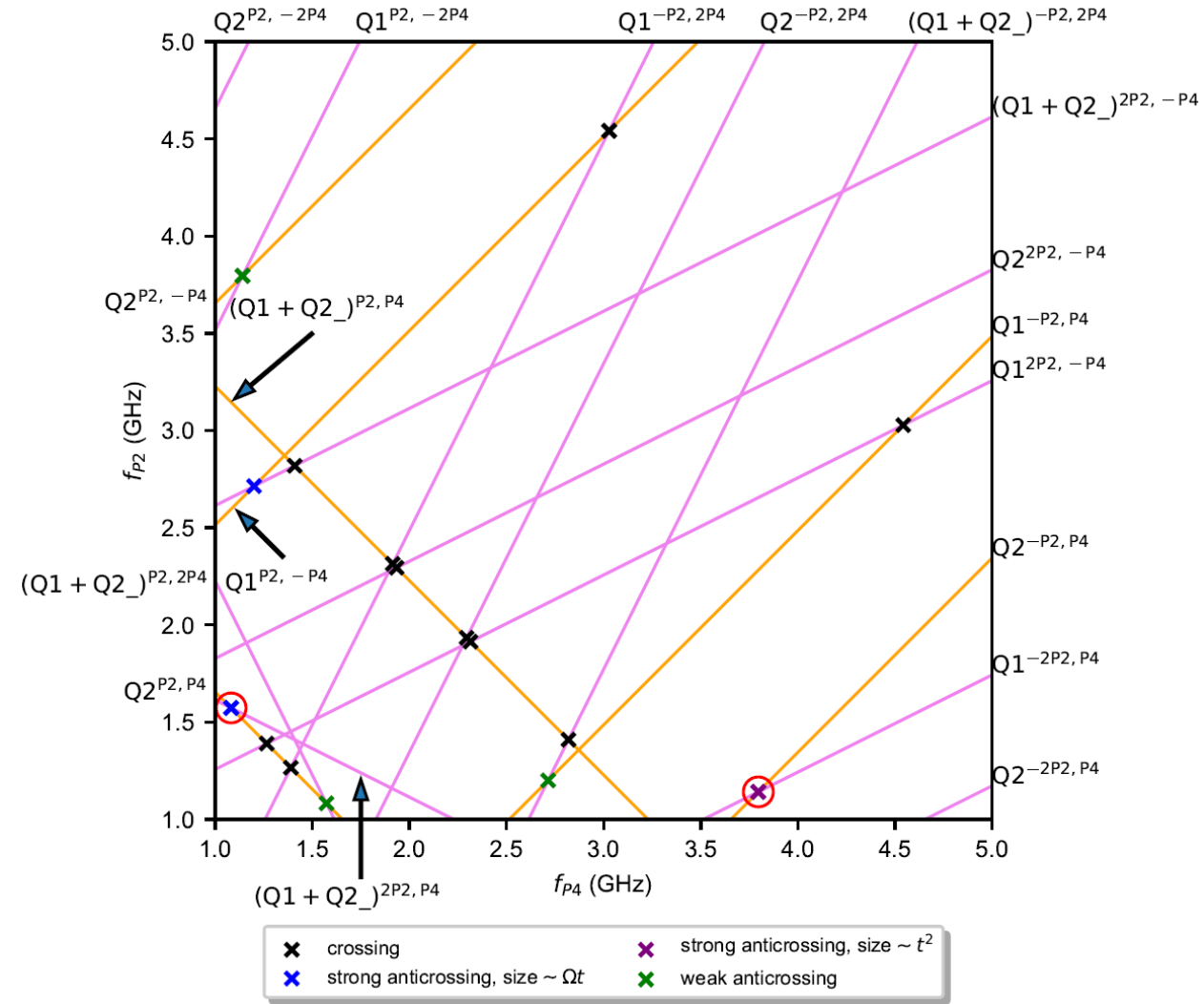
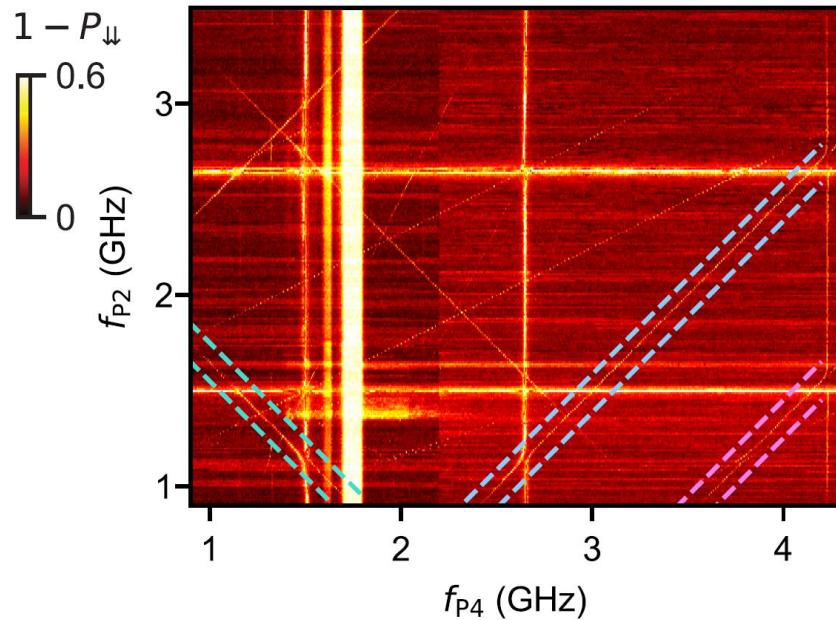


Full spectrum: include 3-photon excitations

Pulse scheme:

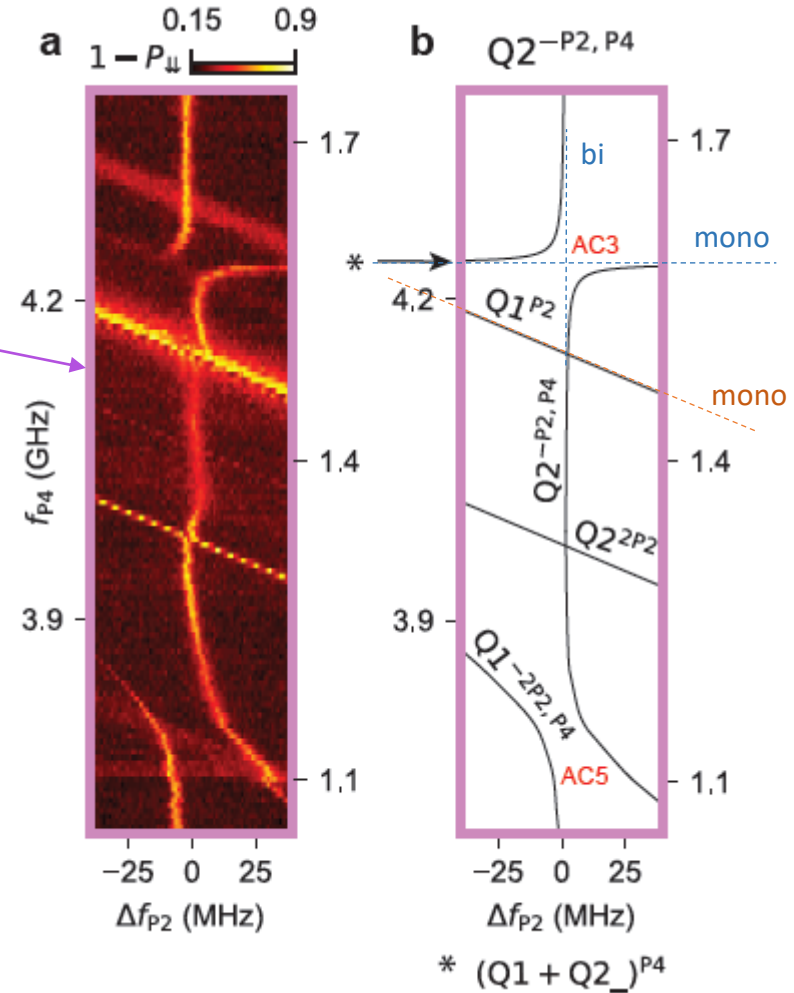
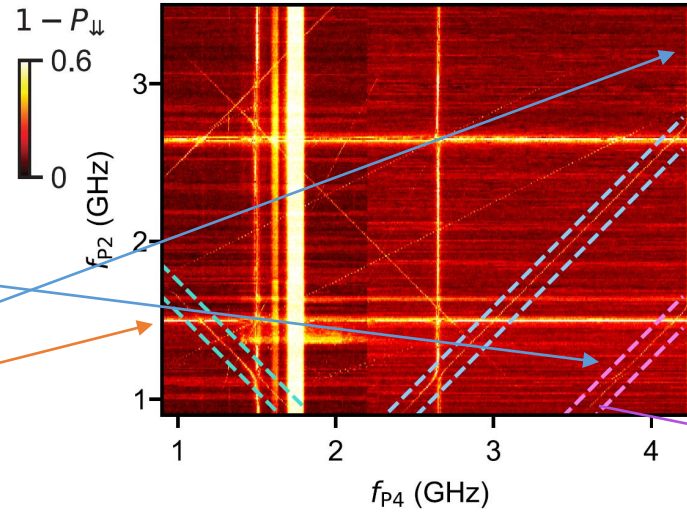


- Resonance between two-photon and single-photon driving with qubit Larmor frequency
- Observed sometimes



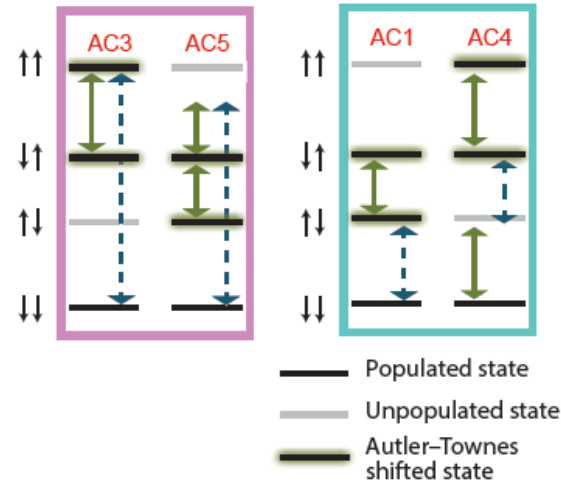
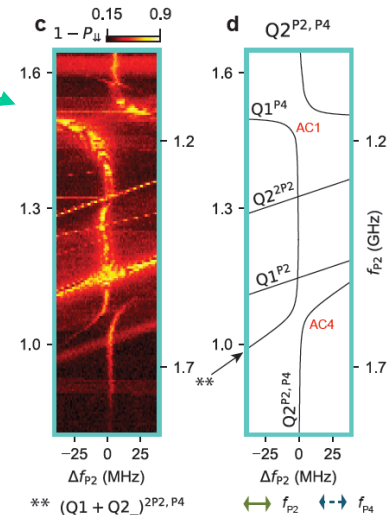
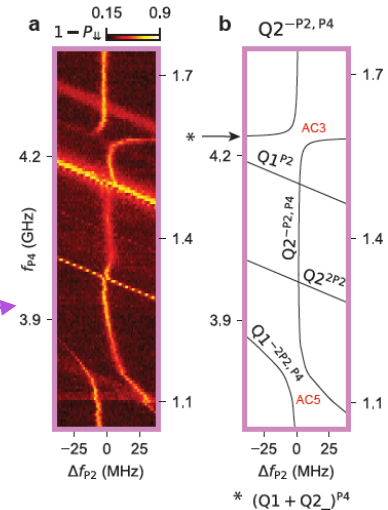
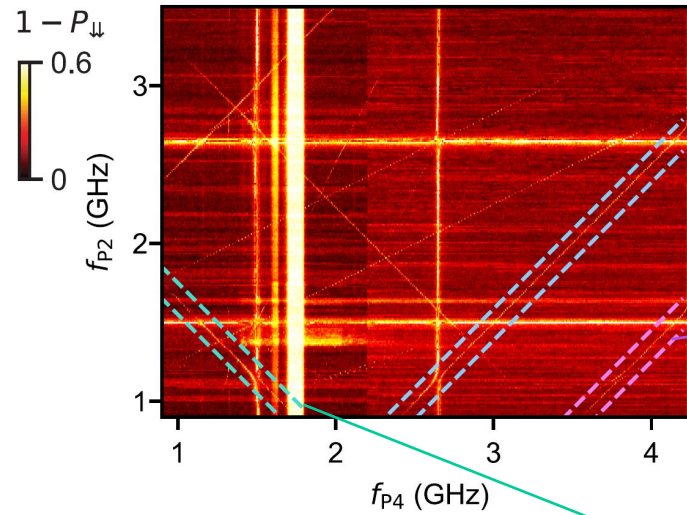
Investigation of anticrossings (I)

- Follow marked transitions closely (window of ± 40 MHz)
- Anticrossing (AC) 3 involves:
 - $|\downarrow\downarrow\rangle \leftrightarrow |\downarrow\uparrow\rangle$ (bichromatic)
 - $|\downarrow\downarrow\rangle \leftrightarrow |\uparrow\uparrow\rangle$ (monochromatic)
 - $|\downarrow\uparrow\rangle \leftrightarrow |\uparrow\uparrow\rangle$ (monochromatic)
- Strong P2 driving dresses up spin states $|\downarrow\uparrow\rangle$ and $|\uparrow\uparrow\rangle$; in rotating frame eigenstates become dressed as $\frac{(|\downarrow\uparrow\rangle \pm |\uparrow\uparrow\rangle)}{\sqrt{2}}$ and exhibit splitting set by Rabi frequency \rightarrow Autler-Townes effect (ac Stark shift)
- Resonance frequencies of the **weaker transitions** are shifted by Rabi frequency of the **stronger transition**



Investigation of anticrossings (II)

- AC3&AC5, AC1&AC4 classified as strong anticrossings (theory in supplementary): first-order dependence on P2 driving and second-order dependence on tunneling amplitudes
- AC1 to AC5: on average spin-conserving tunneling energy $t = (18.1 \pm 1.9) \mu eV$ and spin-flip tunneling energy $\Omega = (14.3 \pm 2.4) \mu eV$
- Strong driving via P2 induces **photon-dressed spin transition**, which is blocked at resonance due to Autler-Townes shift

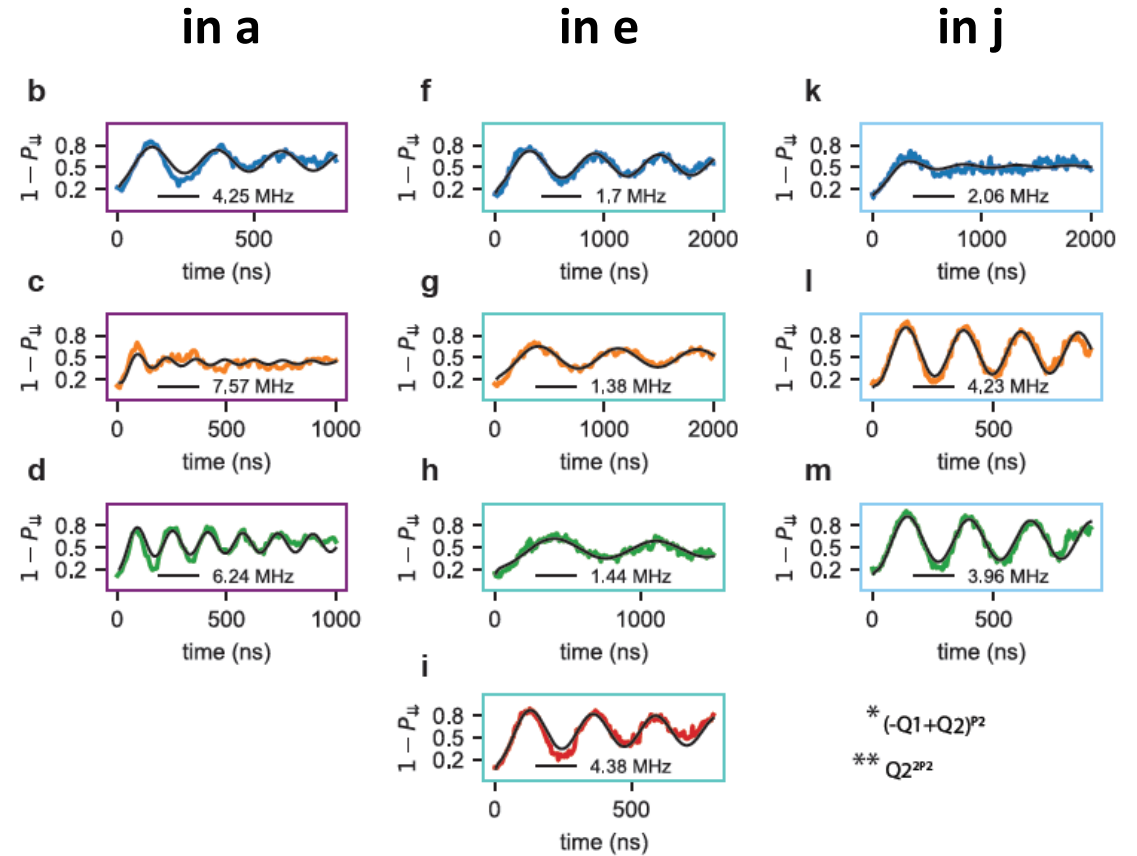
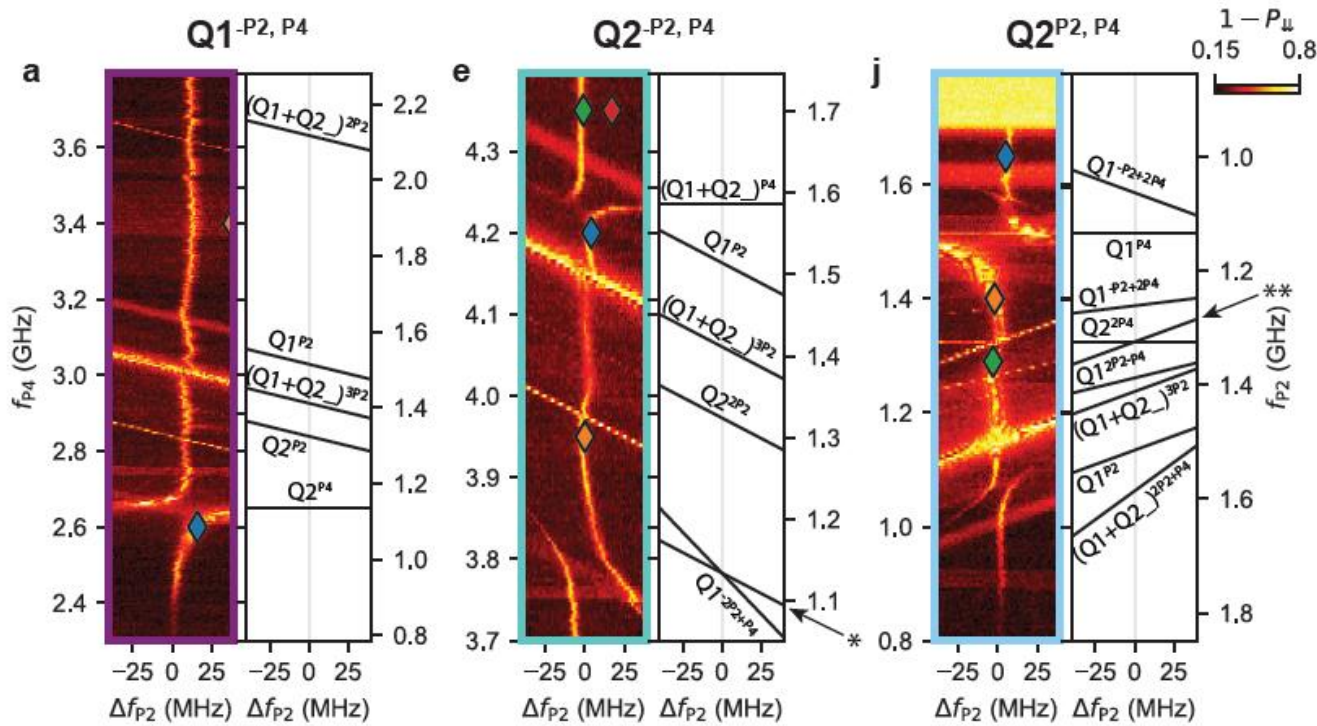


Coherent Rabi control by bichromatic driving

- Rabi oscillations exceed 1 MHz
- Powers: -5 dBm P2, 3 dBm P4

d: as c, but f_{P2} and f_{P4} swapped

Off-resonant points: +4 dBm P2, +2 dBm P4

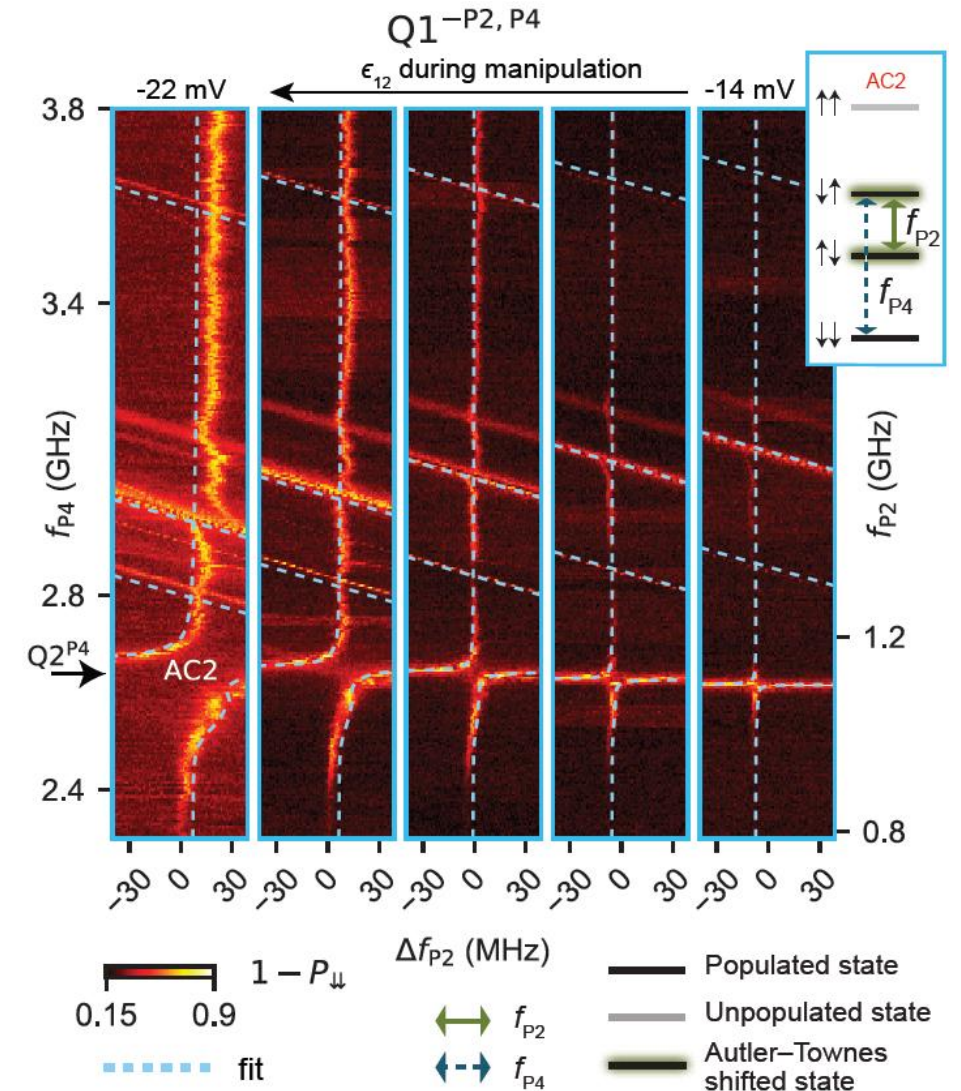
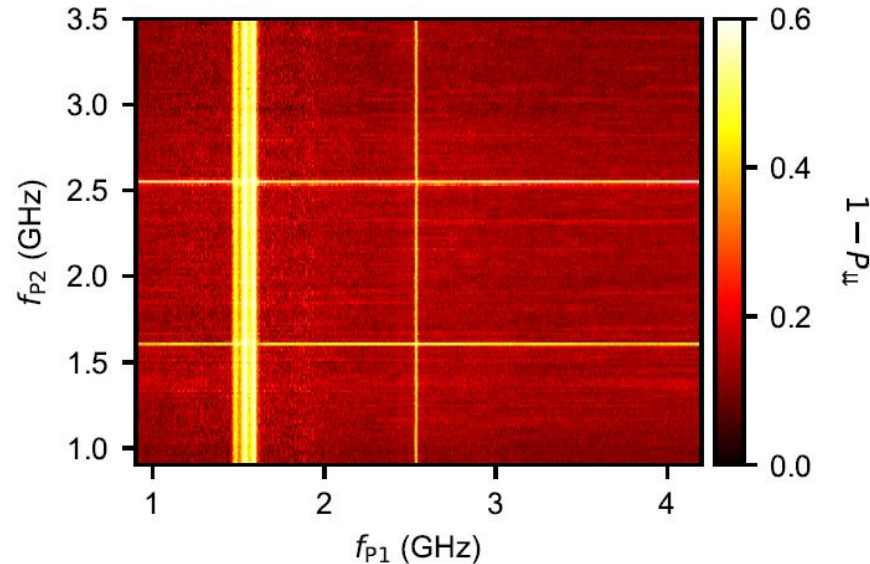


* $(-Q1+Q2)^{P2}$
 ** $Q2^{2P2}$

Changing detuning voltage

- Anticrossing diminishes in size as detuning approaches $\epsilon_{12} \sim 0$
- Bichromatic and monochromatic resonance lines fade, indicating reduced efficiency of bichromatic operations as $\epsilon_{12} \rightarrow 0$
- Supports fundamental role of **virtual interdot transitions** as underlying driving mechanism

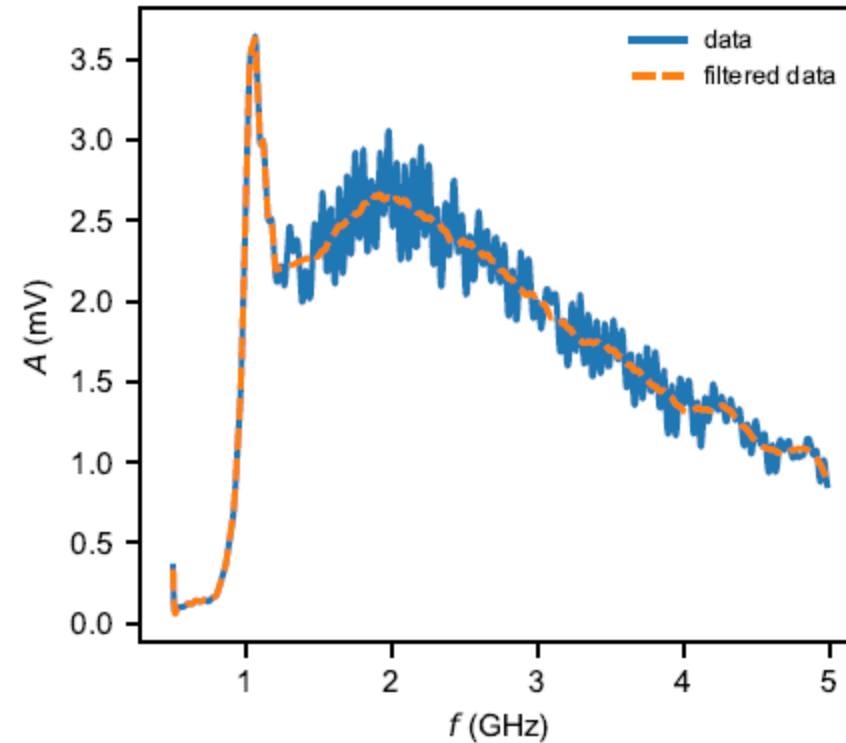
Bichromatic spectroscopy at 0 detuning:



- Demonstration of bichromatic control approach, mapping of different transitions & investigation of anticrossing strengths
- Dependence on detuning highlights importance of interdot motion in obtaining bichromatic&monochromatic driving
- Outlook: Optimize bichromatic driving by tuning parameters such as interdot coupling







Supplementary Figure 5. Attenuation caused by diplexer and fridge cables. Amplitude of the signal arriving at the device level considering $P_{P_4} = 2.5$ dBm. The signal of P2 with $P_{P_2} = -6$ dBm is approximately the same since it has 8.5 dB less attenuation on the lines. A Savitzky-Golay filter is applied on the data, the result is shown with orange-dashed line.

Model Hamiltonian

Here we describe in details the model Hamiltonian of the two-hole double quantum dot introduced in the main text. The matrix representation of that Hamiltonian reads:

$$H = \begin{pmatrix} -\hbar\delta\omega_z & 0 & 0 & 0 & i\hbar\Omega_z - t_0 & i\hbar\Omega_z - t_0 \\ 0 & \hbar\delta\omega_z & 0 & 0 & i\hbar\Omega_z + t_0 & i\hbar\Omega_z + t_0 \\ 0 & 0 & \hbar\omega_z & 0 & -i\hbar\Omega_x - \hbar\Omega_y & -i\hbar\Omega_x - \hbar\Omega_y \\ 0 & 0 & 0 & -\hbar\omega_z & i\hbar\Omega_x - \hbar\Omega_y & i\hbar\Omega_x - \hbar\Omega_y \\ -i\hbar\Omega_z - t_0 & -i\hbar\Omega_z + t_0 & i\hbar\Omega_x - \hbar\Omega_y & -i\hbar\Omega_x - \hbar\Omega_y & U - \epsilon(t) & 0 \\ -i\hbar\Omega_z - t_0 & -i\hbar\Omega_z + t_0 & i\hbar\Omega_x - \hbar\Omega_y & -i\hbar\Omega_x - \hbar\Omega_y & 0 & U + \epsilon(t) \end{pmatrix}, \quad (\text{S9})$$

where the basis states in order are $|\uparrow, \downarrow\rangle$, $|\downarrow, \uparrow\rangle$, $|\uparrow, \uparrow\rangle$, $|\downarrow, \downarrow\rangle$, $|0, 2\rangle$ and $|2, 0\rangle$. We have defined the symmetric and asymmetric Zeeman splittings, respectively, as $\hbar\omega_z = \frac{1}{2}(g_1 + g_2)\mu_B B$ and $\hbar\delta\omega_z = \frac{1}{2}(g_2 - g_1)\mu_B B$, where g_1 and g_2 are the g -factors of Q1 and Q2 dot, μ_B is the Bohr magneton and B is the magnetic field. The g -factors are assumed to depend linearly on the virtual plunger gate voltages vP1 and vP2:

$$g_1 = g_{1,0} + A_1 \text{vP1} + B_1 \text{vP2}, \quad g_2 = g_{2,0} + A_2 \text{vP1} + B_2 \text{vP2}. \quad (\text{S10})$$

The on-site Coulomb repulsion energy is denoted by U . The spin-independent interdot tunneling amplitude is described by t_0 , and spin-dependent tunneling due to spin-orbit interaction is characterised by the vector $\Omega = (\Omega_x, \Omega_y, \Omega_z)$.

We anticipate that the positions of the monochromatic and bichromatic transitions in the (f_{P2}, f_{P4}) frequency plane, as well as the resonance anticrossing curves in that plane, can be described in terms of the following two combined tunneling amplitudes:

$$te^{i\Phi} = t_0 + i\hbar\Omega_z, \quad \Omega e^{i\Phi_c} = \hbar(\Omega_y + i\Omega_x), \quad (\text{S11})$$

where $t, \Omega > 0$ and $\Phi, \Phi_c \in [0, 2\pi)$. We call t and Ω the spin-probability conserving and spin-probability flipping tunnelings. The results of our present analysis are insensitive to the phase angles Φ and Φ_c . However, these phase angles are relevant in the sense that they affect the fine structure of the resonance anticrossings, and contribute to interference effects if additional driving mechanisms are taken into account, besides the detuning modulation in H .

In Eq. (S9), the on-site energy difference (*detuning*) is expressed from the virtual plunger gate voltages as:

$$\epsilon(t) = \epsilon + \delta\epsilon(t) = \alpha(\text{vP1} - \text{vP2} + \delta\text{vP1}(t) - \delta\text{vP2}(t)). \quad (\text{S12})$$

Here, ϵ is the static component of the detuning, and $\delta\epsilon(t)$ is the detuning modulation, furthermore, $\alpha = 0.0917$ eV/V is the lever arm, and $\delta\text{vP1}(t)$ and $\delta\text{vP2}(t)$ are the ac components of the virtual plunger gate voltages describing the driving signals. The lever-arm α describes how much the quantum dots' on-site energies are changed by the virtual plunger gate voltages, and the lever arm is the same for plungers vP1 and vP2 with good approximation. The modulations of the virtual plunger gate voltages $\delta\text{vP1}(t)$ and $\delta\text{vP2}(t)$ depend on the ac signals on P4 and P2:

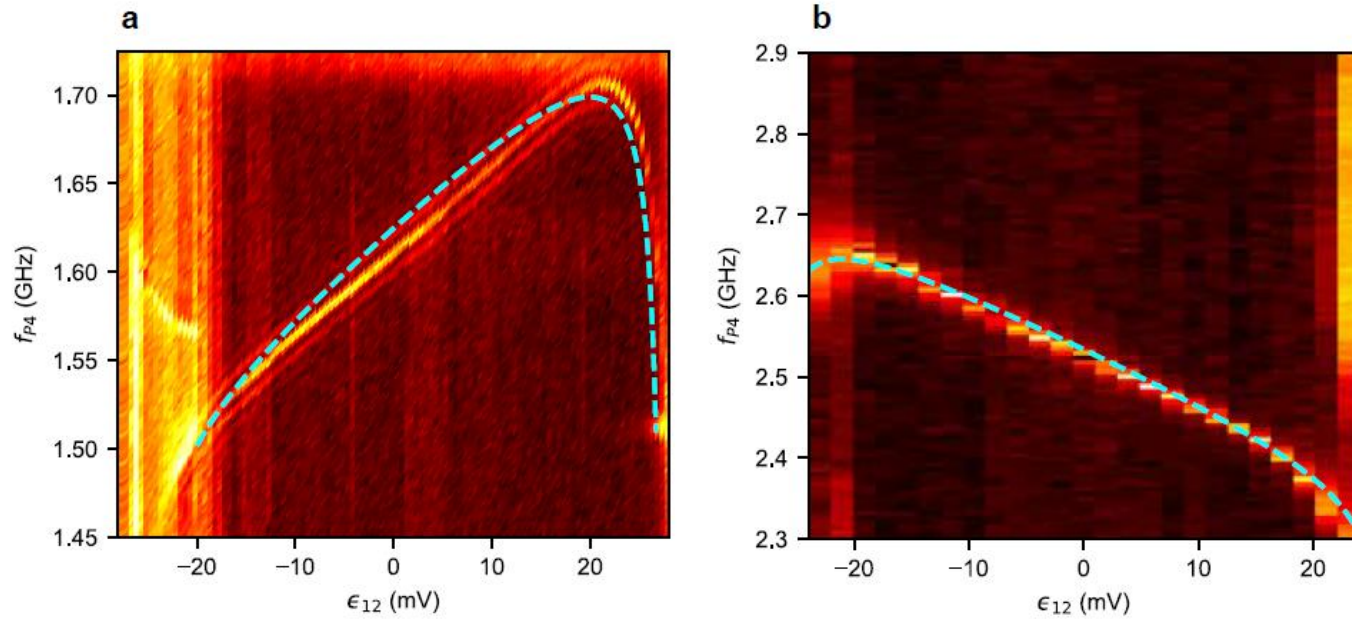
$$\begin{pmatrix} \text{vP1}(t) \\ \text{vP2}(t) \end{pmatrix} = \begin{pmatrix} M_{12} & M_{14} \\ M_{22} & M_{24} \end{pmatrix} \begin{pmatrix} E_{P2} \cos \omega_2 t \\ E_{P4} \cos \omega_4 t \end{pmatrix}, \quad (\text{S13})$$

where E_{P2} and E_{P4} denote actual plunger gate voltages on P2 and P4. Hence, the detuning modulation $\delta\epsilon(t)$ can be written as:

$$\delta\epsilon(t) = \alpha(M_{12} - M_{22})E_{P2} \cos \omega_2 t + \alpha(M_{14} - M_{24})E_{P4} \cos \omega_4 t = \epsilon_{P2} \cos \omega_2 t + \epsilon_{P4} \cos \omega_4 t, \quad (\text{S14})$$

where we introduced $\epsilon_{P2} = \alpha(M_{12} - M_{22})E_{P2}$ and $\epsilon_{P4} = \alpha(M_{14} - M_{24})E_{P4}$, while $M_{12} = 0.446$, $M_{22} = 1.231$, $M_{14} = 0.353$ and $M_{24} = 0.234$, the corresponding matrix elements in Eq. S1.

Parameters of static Hamiltonian



Supplementary Figure 6. Inference of the parameters of the static Hamiltonian from EDSR spectroscopy. a. Experimental EDSR spectroscopy data showing the resonance frequency f_{Q1} as function of detuning voltage ϵ_{12} . The pulse sequence consisted of a pulse on P4 with $t_{\text{mw,P4}} = 118$ ns and $P_{P4} = -1$ dBm, where its frequency f_{P4} has been swept from 1.45 to 1.75 GHz. Before and after this pulse we apply another fixed pulse on P2 with $f_{\text{mw,P2}} = 2.67$ GHz, $P_{P2} = -15$ dBm and $t_{\text{mw,P2}} = 34$ ns, which creates a superposition state at $\epsilon_{12} = -20$ mV. Dashed line shows the fit of Eq. S15 on the data. b. Experimental EDSR spectroscopy data showing the resonance frequency f_{Q2} as function of the detuning voltage ϵ_{12} . The pulse sequence consisted of a pulse on P2 with $t_{\text{mw,P2}} = 118$ ns and $P_{P2} = -5$ dBm, where its frequency f_{P4} has been swept from 2.3 to 2.9 GHz. No additional pulse has been applied. Dashed line shows the fit of Eq. S16 on the data.

The fitting procedure is as follows. We order the spectrum of the static part of H as $E_1 < E_2 < E_3 < E_4 < E_5 < E_6$. Using second-order Schrieffer-Wolff transformation [S1] on the (1,1) charge subspace, we obtain approximate results for the resonance frequencies f_{Q1} and f_{Q2} :

$$hf_{Q1} = E_2 - E_1 \approx \mu_B B \left[g_{1,0} + \frac{A_1 - B_1}{2} \epsilon_{12} \right] + 2 \frac{\Omega^2 - t^2}{U} \frac{1}{1 - \frac{\alpha^2}{U^2} \epsilon_{12}^2}, \quad (\text{S15})$$

$$hf_{Q2} = E_3 - E_1 \approx \mu_B B \left[g_{2,0} + \frac{A_2 - B_2}{2} \epsilon_{12} \right] + 2 \frac{\Omega^2 - t^2}{U} \frac{1}{1 - \frac{\alpha^2}{U^2} \epsilon_{12}^2}. \quad (\text{S16})$$

Note that both formulas contain four fitting parameters, and two of those fitting parameters are the same. We first fit Eq. (S15) on the resonance curve shown in Suppl. Fig. 6a, and hence obtain these values:

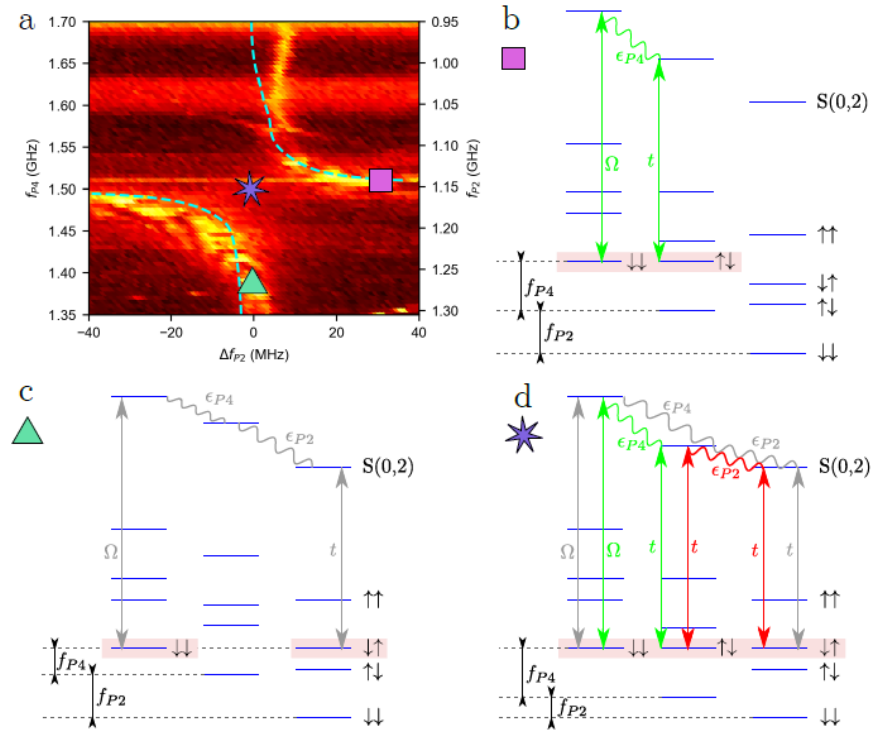
$$g_{1,0} = 0.174, \quad A_1 - B_1 = 1.043 \cdot 10^{-3} \frac{1}{\text{mV}}, \quad (\text{S17})$$

$$\frac{\Omega^2 - t^2}{U} = -0.0474 \mu\text{eV}, \quad \frac{\alpha}{U} = 0.0358 \frac{1}{\text{mV}}. \quad (\text{S18})$$

Then, we insert the parameter values in Eq. (S18) into Eq. (S16), and infer the remaining two parameters of (S16) by fitting that on the resonance curve of Suppl. Fig. 6b:

$$g_{2,0} = 0.271, \quad A_2 - B_2 = 1.426 \cdot 10^{-3} \frac{1}{\text{mV}}. \quad (\text{S19})$$

Floquet theory description



Supplementary Figure 7. Electrically driven monochromatic and bichromatic transitions, and their resonance anticrossing, described using Floquet theory. **a.** Measured data of the anticrossing AC1 of the monochromatic single-photon transition $Q1^{P4}$ and the bichromatic two-photon transition $Q2^{P2,P4}$. Dashed lines show the result of fitting Eq. (S32). Marked points indicate monochromatic (purple square) and bichromatic (green triangle) transitions, and the centre of the resonance anticrossing (blue star) at the intersection of the monochromatic and bichromatic resonances. **b.** Floquet level diagram of monochromatic transition $Q1^{P4}$. The two degenerate Floquet levels are $|\downarrow\downarrow, 0, 0\rangle$ and $|\uparrow\downarrow, 0, -1\rangle$, which are connected by the electric-field matrix element of plunger P4, ϵ_{P4} , and the two tunnelings t and Ω . **c.** Floquet level diagram of bichromatic transition $Q2^{P2,P4}$. The two degenerate Floquet levels are $|\downarrow\downarrow, 0, 0\rangle$ and $|\downarrow\uparrow, -1, -1\rangle$, which are connected by the two electric-field matrix elements ϵ_{P2} , ϵ_{P4} and the two tunnelings Ω and t . **d.** Floquet level diagram of the anticrossing of $Q2^{P2,P4}$ with $Q1^{P4}$. The anticrossing is formed when the conditions of both monochromatic and bichromatic transitions are fulfilled, therefore the three Floquet levels mentioned above are degenerate. For simplicity, only half of the pathways through the $S(0,2)$ are shown, but the other half and the ones going through $S(2,0)$ look similar.

Various tables ☺

Transition	Formula	Measured frequency (MHz)	Calculated frequency (MHz)
$Q2^{P2}$	$f_R = \frac{4\epsilon_{P2}\epsilon U\Omega t}{h(U^2 - \epsilon^2)^2}$	20.66 ± 0.05	19.0 ± 5.1
$Q2_{-}^{P2}$	$f_R = \frac{4\epsilon_{P2}\epsilon U\Omega t}{h(U^2 - \epsilon^2)^2}$	22.1 ± 0.1	18.6 ± 5.0
$Q1^{P4}$	$f_R = \frac{4\epsilon_{P4}\epsilon U\Omega t}{h(U^2 - \epsilon^2)^2}$	11.76 ± 0.04	2.9 ± 0.8
$Q1_{-}^{P4}$	$f_R = \frac{4\epsilon_{P4}\epsilon U\Omega t}{h(U^2 - \epsilon^2)^2}$	5.65 ± 0.02	3.0 ± 0.8
$Q1^{-P2,P4}$	$f_R = \frac{2\epsilon_{P2}\epsilon_{P4}U(U^2 + 3\epsilon^2)\Omega t}{h(U^2 - \epsilon^2)^3}$	6.24 ± 0.04	0.59 ± 0.16
$Q2^{-P2,P4}$	$f_R = \frac{2\epsilon_{P2}\epsilon_{P4}U(U^2 + 3\epsilon^2)\Omega t}{h(U^2 - \epsilon^2)^3}$	1.695 ± 0.008	0.40 ± 0.11
$Q1^{P2,P4}$	$f_R = \frac{2\epsilon_{P2}\epsilon_{P4}U(U^2 + 3\epsilon^2)\Omega t}{h(U^2 - \epsilon^2)^3}$	4.23 ± 0.01	0.65 ± 0.17

Supplementary Table 2. Comparison of measured and calculated monochromatic and bichromatic Rabi frequencies. Theoretical Rabi frequencies of different monochromatic and bichromatic transitions were calculated with Floquet theory and Schrieffer-Wolff transformation, using the spin-conserving tunneling t and spin-flip tunneling Ω obtained from fitting the resonance anticrossings. The errors of the calculated frequencies originate from the uncertainties of the average spin-conserving and spin-flip tunneling, see Supplementary Table 7.

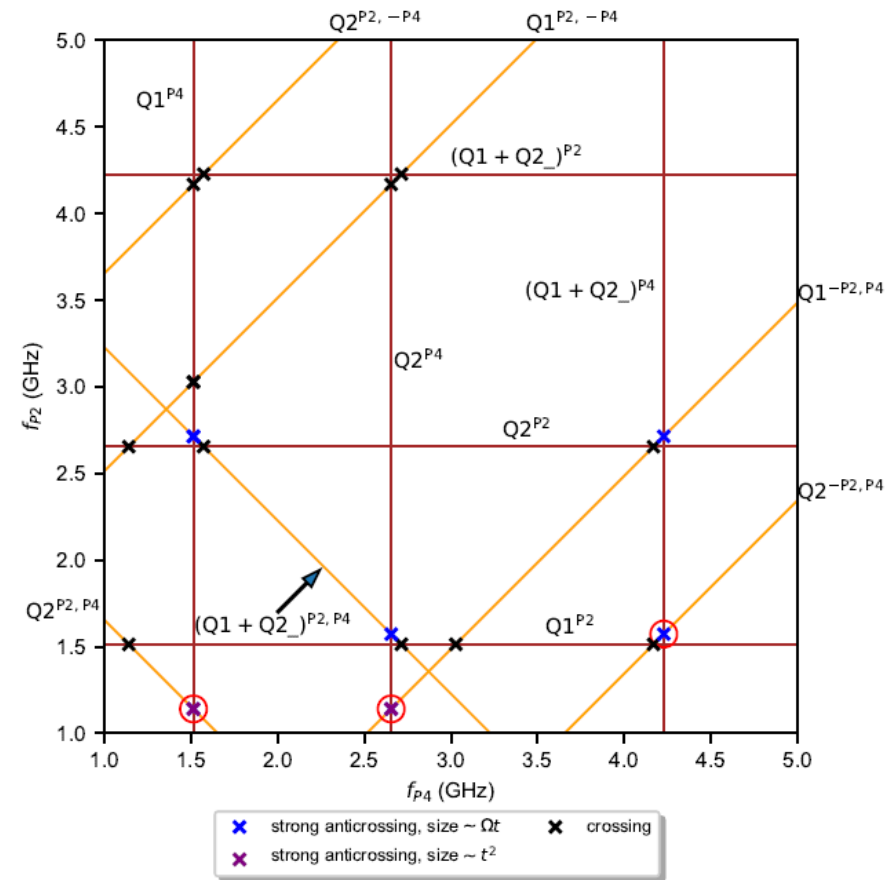
Anticrossing	Resonance (1)	$(n_{P2}^{(1)}, n_{P4}^{(1)})$	Resonance (2)	$(n_{P2}^{(2)}, n_{P4}^{(2)})$	Anticrossing size
AC1	$Q1^{P4}$	(0,1)	$Q2^{P2,P4}$	(1,1)	$\propto \frac{\epsilon_{P2}t^2}{U^2}$
AC2	$Q2^{P4}$	(0,1)	$Q1^{-P2,P4}$	(-1,1)	$\propto \frac{\epsilon_{P2}t\Omega}{U^2}$
AC3	$(Q1 + Q2_{-})^{P4}$	(0,1)	$Q2^{-P2,P4}$	(-1,1)	$\propto \frac{\epsilon_{P2}t^2}{U^2}$
AC4	$Q2^{P2,P4}$	(1,1)	$(Q1 + Q2_{-})^{2P2,P4}$	(2,1)	$\propto \frac{\epsilon_{P2}t\Omega}{U^2}$
AC5	$Q2^{-P2,P4}$	(-1,1)	$Q1^{-2P2,P4}$	(-2,1)	$\propto \frac{\epsilon_{P2}t^2}{U^2}$

Supplementary Table 3. Experimentally observed resonance anticrossings.

Transition	1-photon	2-photon (bichromatic)	2-photon (monochromatic)	3-photon (monochromatic)	3-photon (bichromatic)
1-photon	C	SAC, C	C	C	C
2-photon (bichromatic)		WAC, C	C	C	SAC, WAC, C
2-photon (monochromatic)			C	C	SAC, WAC, C
3-photon (monochromatic)				C	WAC, C
3-photon (bichromatic)					WAC, C

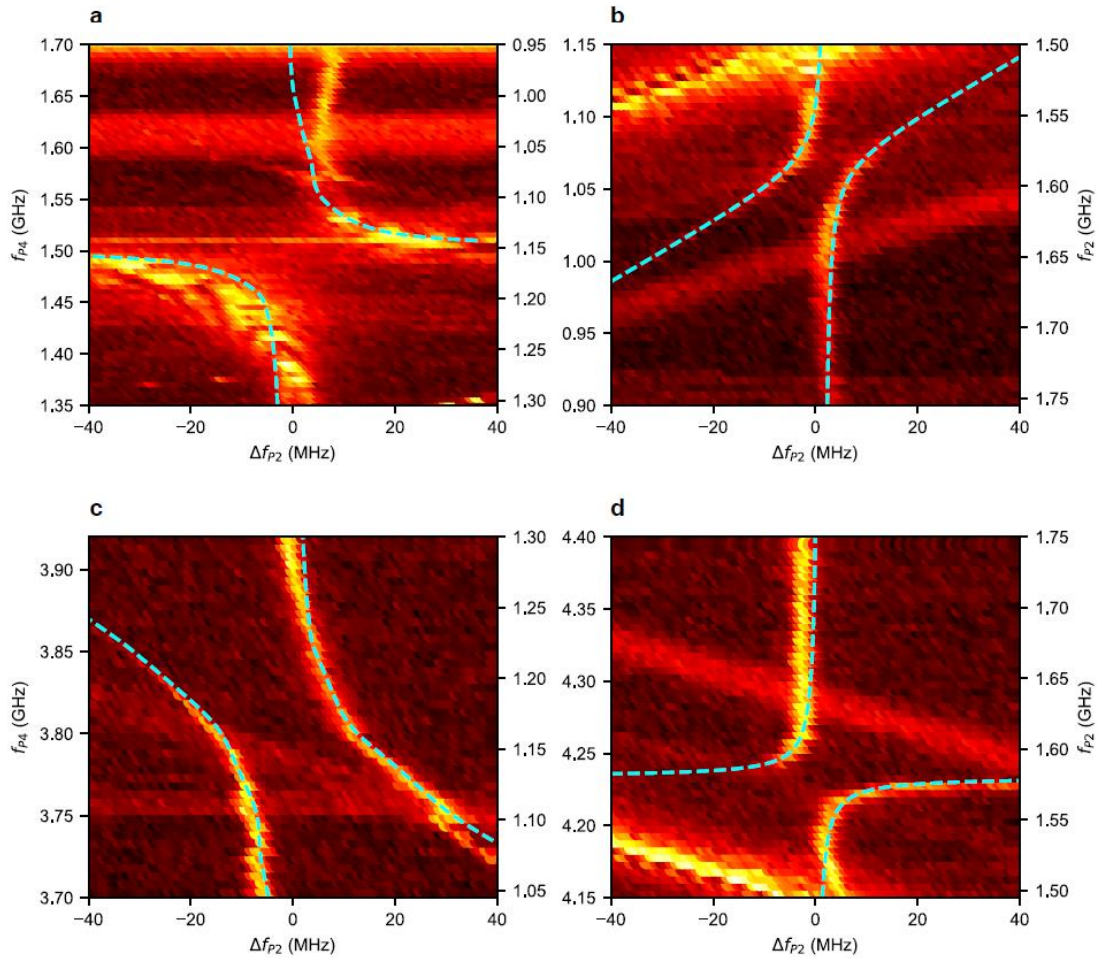
Supplementary Table 4. Anticrossings and crossings of different transitions. The intersection of monochromatic and bichromatic processes with photon numbers from one to three can form strong anticrossings (SAC), weak anticrossings (WAC) and crossings (C).

More about (anti)crossings



Supplementary Figure 8. Crossings and anticrossings of single-photon monochromatic and two-photon bichromatic processes. All possible single-photon monochromatic (brown lines) and two-photon bichromatic processes (yellow lines) are shown which are observable in the shown frequency range. Strong anticrossings mediated by Ωt tunnelings are shown with blue, while the strong anticrossings mediated by t^2 can be seen with purple markers. The intersections which result in crossings are marked with black. The red circles indicate anticrossings which are investigated in detail experimentally and theoretically.

More about (anti)crossings (II)



Supplementary Figure 10. Resonance anticrossings: experiment and theory. Experimental data is identical to that of Fig. 3 of the main text. a. Resonance anticrossing AC1, experimental data and the fitted theoretical resonance curve (dashed) described by Eq. (S32). b. The fit of Eq. (S39) on resonance anticrossing AC4. c. The fit of Eq. (S45) on resonance anticrossing AC5. d. The fit of Eq. (S51) on resonance anticrossing AC3.

ϵ_{12} (mV)	x_0 (MHz)	y_0 (GHz)	t (μeV)
-14	-7.420	2.617	14.99
-16	-5.585	2.628	16.54
-18	-0.899	2.644	18.59
-20	6.574	2.652	18.91
-22	7.035	2.666	16.53

Supplementary Table 5. Fitting parameters of anticrossing AC2.

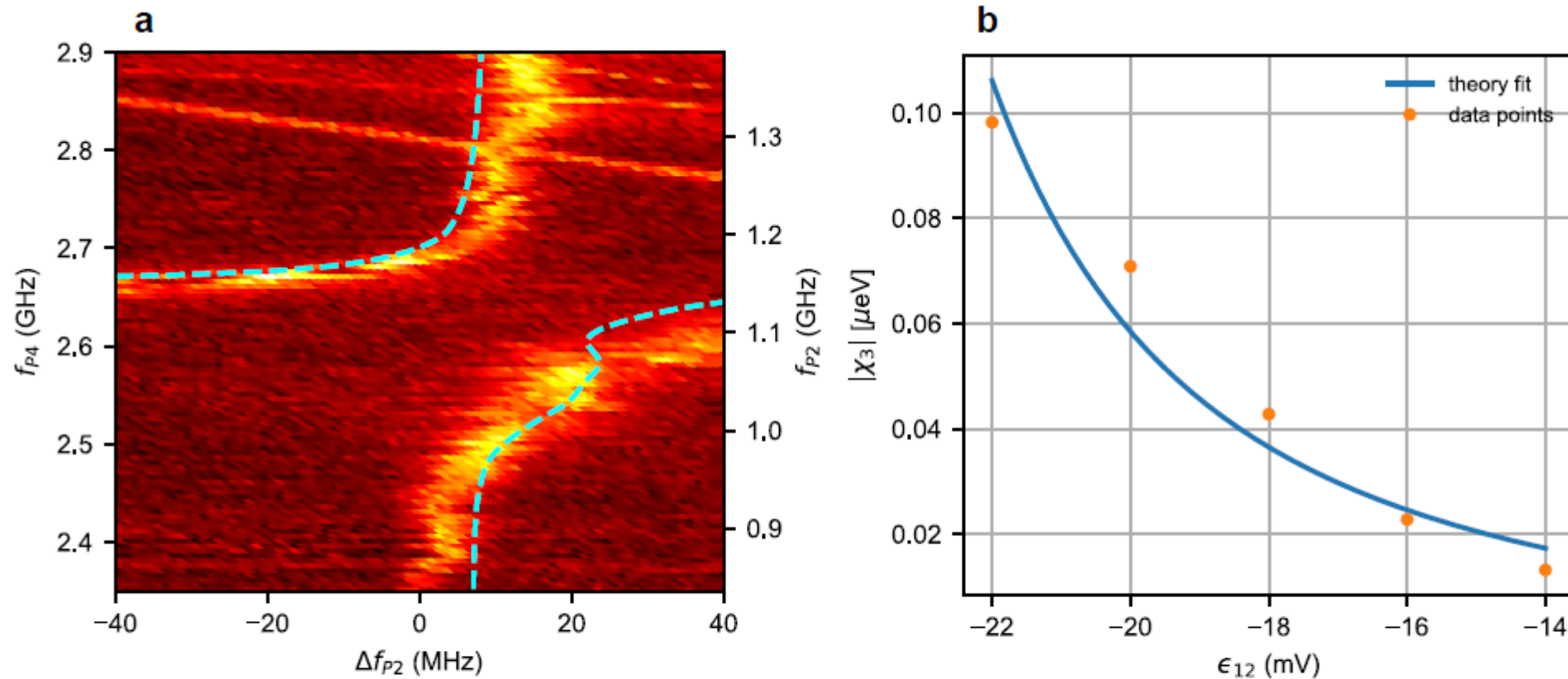
Anticrossing	ϵ_{12} (mV)	t (μeV)	Ω (μeV)
AC1	-20	20.42	17.19
AC2	-22	16.53	12.32
AC2	-20	18.91	15.37
AC2	-18	18.59	14.98
AC2	-16	16.54	12.34
AC2	-14	14.99	10.18
AC3	-20	17.85	14.05
AC4	-20	17.77	13.95
AC5	-20	21.26	18.18

Supplementary Table 6. Calculated spin-conserving and spin-flip tunnelings using the different fitted anticrossings. Using Eq. (S18), the relation between t and Ω the tunneling amplitudes can be calculated from the fit results of the anticrossings.

Average t [μeV]	Average Ω [μeV]
18.1 ± 1.9	14.3 ± 2.4

Supplementary Table 7. Average hopping parameters. An average t and Ω value was calculated using the values from Tab. 6.

More about (anti)crossings (III)



Supplementary Figure 11. Detuning dependence of anticrossing AC2. a. Anticrossing AC2 at $\epsilon_{12} = -22$ mV point and the fitted theoretical resonance line Eq. S58 b. The absolute values of χ_3 calculated at a constant driving ($\epsilon_{P2}(f_{P2} = 1.1$ GHz)) as a function of detuning voltage ϵ_{12} ranging from -22 mV to -14 mV with orange markers. The absolute value of χ_3 (see Eq. S55) is fitted on the datapoints, the result of the fit can be seen with blue line.